ADDITIVE MANUFACTURING TECHNOLOGY POWERING A NOVEL ENHANCEMENT IN ELECTRIC POWER CONVERSION

Edoardo Sech[b], Samuele Nizzardo[a], Daniele De Gregorio[a], Francesco Tripaldi[a], Lino di Leonardo[a], Nicola Bianchi[a], Anna Stoppato[a], Alberto Benato[a]

[a] *University of Padova, Department of Industrial Engineering, Padova, Italy*
[b] *University of Padova, Department of Industrial Engineering, Padova, Italy, edoardo.sech@phd.unipd.it, CA*

Abstract:
This work investigates a novel power-conversion-oriented winding technology that significantly extends the torque and thermal limits of electric machines. The proposed approach embeds forced liquid cooling directly within additively manufactured hollow copper conductors, effectively decoupling electromagnetic loading from conventional thermal constraints and enabling a step change in achievable torque density. The hollow-conductor architecture allows current densities up to two to three times higher than those of state-of-the-art externally cooled windings ($50 - 70A/mm^2$), resulting in a substantial increase in usable torque. Referring to a high power electric machine, Finite-element electromagnetic analyses have demonstrated that the computed torque density can be increased by 2.5 times using internally cooled windings compared to what is obtained with a conventional hairpin winding and external water jacket, without degradation of magnetic performance. Beyond the performance improvement, the proposed solution introduces a versatile thermal management concept that can be transferred to different machine topologies and operating conditions for high-performance energy conversion systems, owing to the strong enhancement of the heat transfer coefficient. The study combines experimental testing of a manufactured hollow-coil prototype with coupled electromagnetic, thermal, and fluid- dynamic numerical models. Computational fluid dynamics simulations of the internal flow and heat transfer show good agreement with experimental measurements, providing a tool for the investigation of a wide range of working possibilities in terms of cooling fluid, geometry, and electrical load. In addition, a simplified one-dimensional modelling framework is proposed to efficiently explore design configurations and estimate parasitic losses, providing preliminary insights into the overall energy efficiency of systems employing the proposed technology.

Keywords:
Axial flux Motor, CFD, Cooling, Additive Manufacturing.

1. Introduction

The electrification of the transport and industrial sectors is fostering extensive research on electric machines characterised by progressively higher power and torque densities [1]. However, performance improvements are fundamentally limited by thermal management, particularly the heat generated in stator windings, which represent a primary heat source [2]. In this context, the equivalent thermal resistance between the heat source and the coolant is widely recognised as a key bottleneck [3]. The achievement of the design torque and power performance must not exceed the maximum copper insulation temperature; otherwise, it may compromise machine health. If the electrical machine includes permanent magnets (PMs), it is also necessary to avoid irreversible demagnetisation of the PMs themselves. In recent years, several studies have focused on the enhancement of torque density [4] to address the new requirements arising from modern conversion challenges. In this perspective, axial flux machines (AFMs) have gained increasing attention in recent years as a promising alternative to conventional radial flux machines (RFMs), primarily due to their compact geometry, high torque density, and enhanced efficiency potential. Unlike RFMs, AFMs adopt a disc-shaped topology with axial flux paths, enabling a larger mean radius and shorter magnetic circuit, which enhances torque density and reduces core losses. These features make AFMs particularly attractive for emerging applications such as electric vehicles (EVs), aerospace propulsion, and portable power systems, where spatial and weight constraints are critical. Recent developments in materials and manufacturing, such as high-energy permanent magnets, soft magnetic composites (SMCs), and additive manufacturing, have significantly improved the performance and manufacturability of AFMs. For instance, the torque density of state-of-the-art AFMs has reached values as high as 40–60 Nm/kg [5], compared to typical RFMs which often remain below 30 Nm/kg for similar power levels [5].

In this new scenario, conventional cooling strategies often prove inadequate for applications involving high current densities. To dissipate the significant heat generated within the stator slots, researchers have explored a variety of thermal management techniques, which can be broadly categorised into indirect and direct cooling. Indirect cooling methods, such as water-cooled housing jackets and the use of thermally conductive potting resins [6], are widely adopted due to their simplicity. However, their effectiveness is heavily limited by the high thermal resistance of the electrical insulation layers and the ferromagnetic core, which the heat must bypass before reaching the coolant. To overcome these deep-seated thermal barriers, direct cooling approaches—including in-slot cooling channels, end-winding spray cooling, and hollow conductors—have been recently investigated [7,8]. Although these direct methods present a remarkable improvement in heat extraction capabilities, they inherently introduce critical drawbacks: they often compromise the machine's electromagnetic design by reducing the active slot fill factor, and they typically induce severe pressure drops that drastically increase the auxiliary pumping power required, thereby penalising the net efficiency of the system [9]. In this complex scenario, Additive Manufacturing (AM) technologies are emerging as a key enabler to break conventional thermal bottlenecks. Unlike traditional subtractive or casting processes that impose strict limitations on internal cavity designs, AM techniques, such as Selective Laser Melting (SLM), grant unprecedented design freedom [10]. Additive Manufacturing (AM) enables unprecedented design freedom, allowing the integration of conformal cooling channels directly within machine components [11]. This is particularly advantageous for AFMs, where compact geometries impose severe space constraints [12]. This technology enables the fabrication of customised fluid domains, such as lattice structures or variable-section channels, strategically designed to maximise the local heat transfer coefficient exactly at the thermal hotspots, whilst maintaining the overall hydraulic resistance within acceptable limits.

Despite the recognised potential of Additive Manufacturing (AM) in revolutionising the thermal management of electrical machines, a comprehensive integration of AM-enabled conformal cooling specifically tailored for AFMs has thus far been quite unexplored. Most of the existing literature focuses primarily on RFMs or is limited to pure numerical investigations without experimental validation of the complex 3D printed fluid domains. Furthermore, when advanced cooling geometries are proposed, the critical trade-off between improved heat transfer and the consequent penalty of pumping power—a crucial aspect of overall system efficiency—is often overlooked. Additionally, the inherent geometric variations and surface roughness associated with AM processes introduce significant deviations from simplified numerical models, making rigorous experimental validation strictly necessary to evaluate the true performance of these highly integrated cooling solutions.

The present work proposes an innovative thermal management approach to enhance torque density while maintaining high efficiency. A CFD model is developed and validated against experimental data from an additively manufactured prototype. Once the numerical model has been experimentally validated, it serves as a powerful predictive tool. This allows for extensive parametric studies and design optimisations to be performed—drastically reducing the need for costly and time-consuming prototyping—ultimately identifying optimal geometries that maximise heat transfer while minimising pumping power penalties. Finally, the proposed validated methodology lays the groundwork for future investigations into different machine sizes and varied operating conditionss.

2. Materials and Methods

The tested geometry is an additively manufactured hollow conductor copper coil with integrated internal cooling channels (Figure 1). The winding is formed by a stacked, hairpin-like serpentine conductor arranged in multiple parallel layers. Each turn has a flattened rectangular cross-section to maximise the fill factor and reduce electrical resistance, while the turns are spaced to create a sequence of internal slots that act as coolant flow channels running along the length of the conductor. These channels allow the coolant to pass in close proximity to the regions where Joule losses are generated, forming a continuous serpentine channel that ensures uniform coolant distribution across all turns, thereby minimising the thermal path between the heat source and the cooling fluid.

Even though the tested coil has relatively small overall external dimensions, its convoluted geometry results in a comparatively large internal surface area: the overall length reaches approximately $1.87\ m$, and the internal surface, corresponding to the actively heat exchanging one, reaches approximately $40\ dm^2$. Copper density is assumed to be $8960\ kg/m^3$ and thermal conductivity is equal to $400\ W/(m^2K)$. The coil data are reported in Table 1.

Table 1: Hollow Copper coil under test.

Parameter	**Value**
Cross-section area	21.6 mm^2
Inner surface	0.03972 m^2
Length	1.87 m
Copper density	8960 kg/m^3
Thermal conductivity	400 $\text{W/(m}^2\text{K)}$

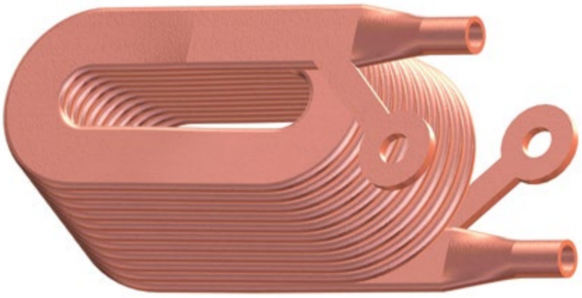

Figure 1: Hollow Copper coil under test.

The philosophy of the testing campaign is based on the comparison of maximum reachable current density for different flow rates, highlighting the potential improvement with respect to traditional levels of working currents. The corresponding levels of powering are hence investigated, together with further increases at a higher flow rate. For the sake of maintaining the meaningfulness of the experiment, typical levels of maximum temperatures allowed to meet insulator safety are respected [13], as well as conditions far from phase change, avoiding problems related to poor distribution of the coolant or consecutive condensation requirements.

The test flow rates remain between $0.25\ l/min$ and $1.2\ l/min$, featuring a current density between $20\ A/mm^2$ and $80\ A/mm^2$.

2.1. Experimental Set-up

The performance of the hollow conductor was tested by means of a specific setup designed to accurately maintain controlled test conditions, as well as to provide a flexible framework for different types of fluids. The experimental campaign aims to quantify possible advantages in the application of this kind of technology using water as a cooling fluid. To do so, a wide range of working conditions have been considered, encompassing different levels of current density and cooling flow rates. Figure 2 illustrates the cooling-fluid circuit, referring to the specific configuration for water tests. The system is supplied by a pressurised fluid line that enters the circuit through a supply conduit. A main valve *V1* regulates the coolant flow rate. Downstream of this component, a by-pass branch controlled by valve *V2* allows for precise partialization. The pressure is monitored upstream of the test section using a manometer *P1*, which is connected to the inlet pipe. Following the test section, the outlet flow is directed toward the discharge manifold, where the downstream pressure is measured using manometer *P2*. The power supply is provided by a high-frequency switching rectifier whose output is stabilised DC current and voltage.

Specific terminals for the delivery of electrical current and refrigerant flow are used to equip the component. Temperature acquisition was possible using PT100 thermocouples.

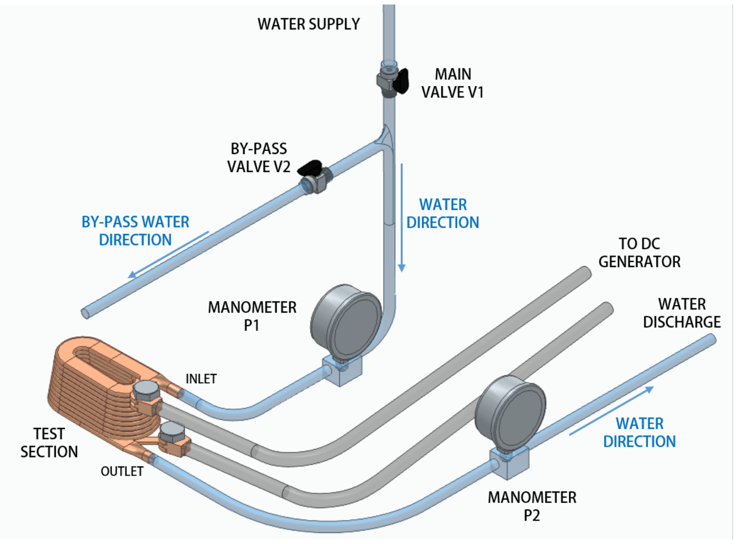

Figure 2: Experimental Test Setup for water cooling.

3. Numerical Set-up

CFD enables the detailed evaluation of thermal and fluid fields across various geometries without physical prototyping. This study adopts a steady-state Reynolds-Averaged Navier-Stokes (RANS) framework, providing a reliable and validated balance between computational efficiency and accuracy for assessing the component's thermal performance. The commercial software ANSYS [14] was adopted for modelling the conjugate thermal-fluid dynamics of the configuration experimentally tested. The fundamental governing equations, such as the continuity, momentum, and energy equations, which are the basis for the solver, are as follows:

$$\frac{\partial \rho}{\partial t} + \nabla \cdot (\rho \vec{U}) = 0 \tag{1}$$

$$\frac{\partial}{\partial t}(\rho \vec{U}) + \nabla \cdot (\rho \vec{U} \vec{U}) = -\nabla \cdot P + \rho \vec{g} + \nabla \cdot \vec{\tau} + \vec{F} \tag{2}$$

$$\frac{\partial}{\partial t}(\rho H) + \nabla \cdot (\rho \vec{U} H) = -\nabla \cdot (K \nabla T) + S \tag{3}$$

A steady state framework was considered, neglecting the initial transient heating up of the fluid and the coil. Different turbulent models were tested, primarily considering two-equation ones. Two-equation turbulence models describe turbulent flows by solving transport equations for two separate turbulence quantities, typically the turbulent kinetic energy (k) and a dissipation-related variable such as the dissipation rate (ϵ) or the specific dissipation rate (ω). Efficient modelling of turbulence production and destruction provides an effective representation of flow energy without requiring full resolution of the smallest turbulent scales. The particular shape of these equations is:

$$\frac{\partial(\rho k)}{\partial t} + \frac{\partial(\rho k u_j)}{\partial x_j} = P_k - \rho\varepsilon + \frac{\partial}{\partial x_j}\left[\left(\mu + \frac{\mu_t}{\sigma_k}\right)\frac{\partial k}{\partial x_j}\right] \tag{4}$$

$$\frac{\partial(\rho \varepsilon)}{\partial t} + \frac{\partial(\rho \varepsilon u_j)}{\partial x_j} = C_{\varepsilon 1}\frac{\varepsilon}{k}P_k - C_{\varepsilon 2}\rho\frac{\varepsilon^2}{k} + \frac{\partial}{\partial x_j}\left[\left(\mu + \frac{\mu_t}{\sigma_\varepsilon}\right)\frac{\partial \varepsilon}{\partial x_j}\right] \tag{5}$$

$$\frac{\partial(\rho \omega)}{\partial t} + \frac{\partial(\rho \omega u_j)}{\partial x_j} = \frac{\gamma\omega}{k}P_k - \beta\rho\omega^2 + \frac{\partial}{\partial x_j}\left[\left(\mu + \frac{\mu_t}{\sigma_\omega}\right)\frac{\partial \omega}{\partial x_j}\right] \tag{6}$$

Equations 4 refer to the turbulent kinetic energy k, equations 5 are about the dissipation rate term ϵ, and equations 6 regard the specific dissipation rate ω.

In this study, multiple turbulence models were evaluated, including the widely used $k-\omega$ and $k-\epsilon$ formulations, to verify the robustness of the numerical predictions. While both traditional two-equation models produced reasonable agreement with the expected flow behaviour, the most accurate and stable results for the water cooling case were obtained using the GEKO (Generalised $k-\omega$) turbulence model.

This evaluation is based on three different unstructured meshes: coarse (1M elements), medium (3.8 M elements), and fine (7.31M elements). The adopted one is the *fine* mesh because it provides better details of the boundary layer, overcoming the difficulties arising from the small gaps and the sharp changes in the shape of the solid section. A proper inflation on both the coil and fluid sides was adopted, thus enabling direct evaluation of wall flow according to the Y+ value of approximately 1.

Figure 3 represents a schematic view of the boundary conditions selected for this work. The inlet mass flow rate and temperature, in conjunction with the outlet pressure, are specified on the corresponding boundary. Adiabatic boundary conditions are imposed on the external surfaces of the coil, thus ensuring that fully coupled heat exchange between the solid and the inner fluid is considered at the surface interface. The thermal power produced by the Joule effect P_{Spec} as a result of the applied current was modelled as an internal heat generation in the solid domain. Its value is evaluated as $P_{Spec} = P/V_{Coil}$ where P is the delivered electrical power and V_{Coil} is the overall solid volume.

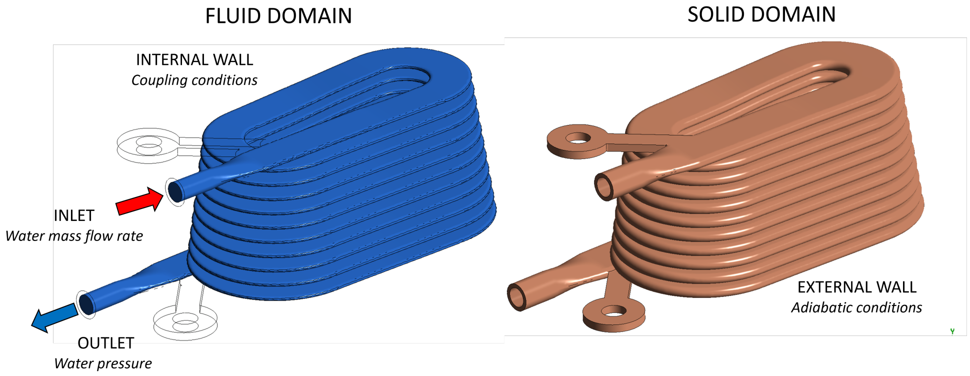

Figure 3: Boundary conditions applied to coil analysis.

3.1. One Dimensional Set-up

As an additional step in the validation of the CFD approach presented in Section 3., the problem was also investigated by performing parametric simulations with built-in components available in the OpenModelica environment. Modelica is an object-orientated language designed for modelling physical systems, and the OpenModelica Connection Editor (OMEdit) is its open-source graphical user interface. It includes several built-in libraries for the modelling of multi-physics systems, as well as generic blocks for mathematical operations and signal processing. In particular, the *Fluid* and *Thermal* libraries provide a set of components that are particularly suitable for representing, with a 1D approach, the experimental setup analysed in this study. The schematic representation of the model developed in OMEdit is presented in Figure 4. It consists of the following components:

- $\mathbf{BC_{inlet}}$: it imposes the boundary conditions at the inlet of the coil, in terms of mass flow rate ($\dot{m}$) and temperature ($\mathrm{T_{in}}$).
- $\mathbf{BC_{outlet}}$: it imposes the boundary conditions at the inlet of the coil, in terms of pressure ($\mathrm{p_{out}}$).
- Pipe: a 1D dynamic model of a generic duct incorporating a heat source. The geometric characteristics of the coils are specified in terms of hydraulic diameter and total length, and the mass, the momentum, and the energy conservation equations are reformulated in their one-dimensional form. The selected heat transfer model computes local heat transfer coefficients

using the Gnielinski correlations.

- HeatFlow: it represents the thermal power transferred to the fluid flow. In this context, the working hypothesis is that the entire thermal power generated by Joule heating in the coil is absorbed by the fluid, while the fraction dissipated to the surrounding air by natural convection is neglected.
- Sensors: they acquire the values of temperature and pressure at the inlet and the outlet of the coil.

The Modelica model was simulated with the same input conditions established during the experimental campaign. The results, presented in Section 4.3., compare the simulation outputs with those obtained from the experiments and the CFD analysis, focusing on the outlet temperature and pressure of the working fluid.

4. Results

4.1. Experimental Results

The test water flow rates stay between 0.25 l/min and 1.2 l/min, featuring a current density between 20 A/mm^2 and 80 A/mm^2.

The coil temperature measurement is evaluated by means of resistance variations, i.e. the voltage at the coil's terminals and the imposed current. The electrical resistance of the coil *R*, depends on temperature T and can be described by the linear relationship:

$$R = R_0 + \alpha \cdot (T - T_0) \tag{7}$$

where R_0 and T_0 are the resistance and temperature values measured before the start of the tests, at ambient temperature, while α is imposed equal to $0.004\ \Omega/K$. The temperature of the copper, evaluated using equation 7, and reported in the data corresponds to an average temperature rise, with considerable changes along the coil, as observed in Figure 5.

The water outlet temperature is reported in Figure 6 while varying the supply current density. A quadratic relationship can be observed, closely resembling the proportionality to Joule losses. It is trivial to observe the better performance demonstrated at higher flow rates in comparison to lower ones.

At low flow rates (e.g. $0.25\ l/min$), the outlet temperature increases rapidly beyond approximately 20–$30\ A/mm^2$, indicating a limited heat-removal capability. Increasing the water flow rate progressively reduces the temperature gradient, with the 1.00 and $1.20\ l/min$ curves maintaining notably lower outlet temperatures across the full current-density range. Referring to the specific case of

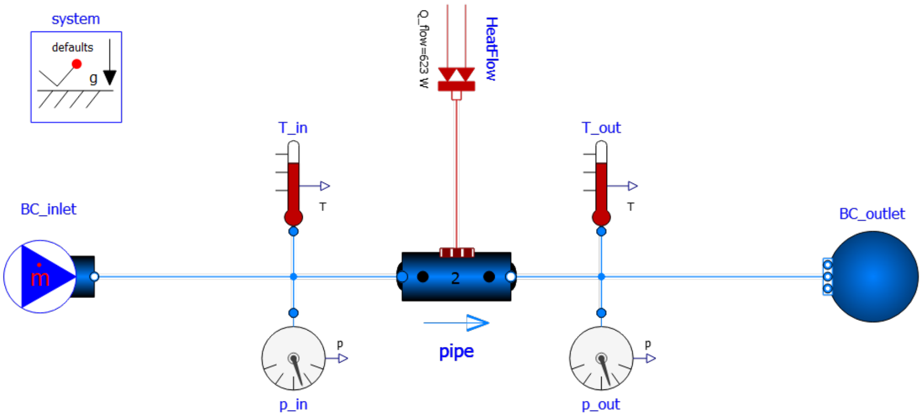

Figure 4: Scheme of the OMEdit model presented in Section 3.1.

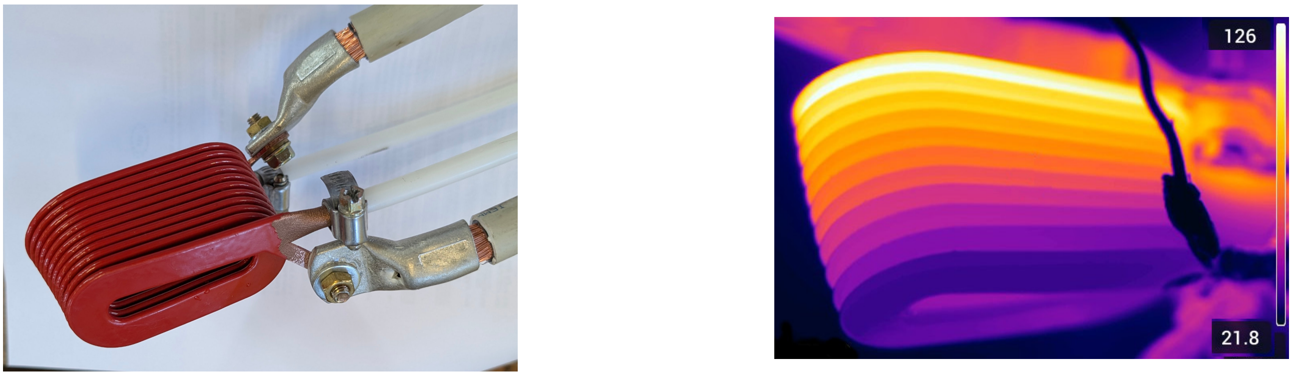

Figure 5: On the left, coil under test connected to power and coolant supply. On the right, example of temperature distribution along the coil during a test.

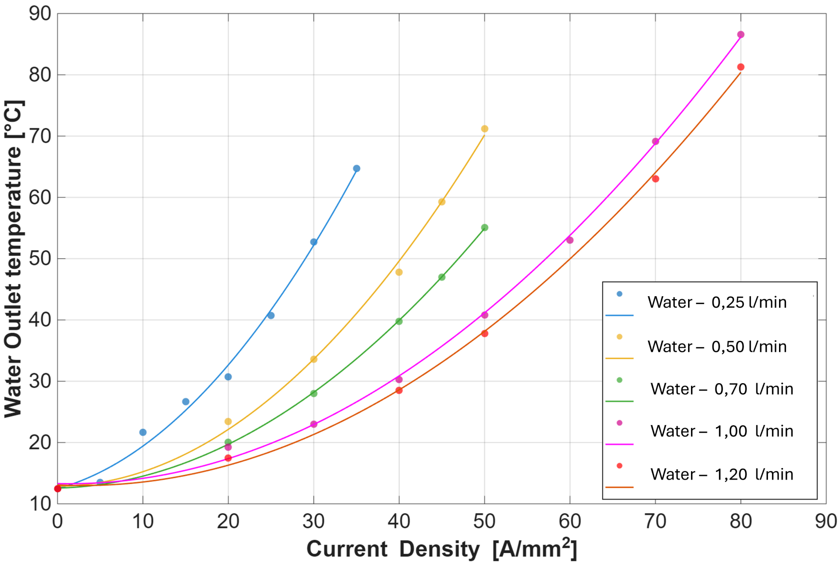

Figure 6: Water Outlet temperature as a function of Current density for different cooling flow rates.

$50\ A/mm^2$, a reduction of more than 30° is observed when the flow rates move from $0.25\ l/min$ to $1.2\ l/min$. Different maximum levels of current density are tested to avoid getting too close to the phase change threshold, enabling a comprehensive assessment of the limits of this cooling technique. It is crucial to observe that considerably higher levels of current density are reached in the test compared to the usual values adopted in electric machinery([5]), while cooling flow rates remain low and consistent with other fluid cooled techniques already existing. The big companies in the sector, consistently advancing in this field, refer to flow rates in the most common water cooled applications, particularly water jacket ones, which are about 10 times higher than the maximum level tested ([15]). In terms of current density levels, values higher than $20-40\ A/mm^2$ are taken into account only for oil-immersed cooling ([15]), introducing significantly different levels of complexity into the system.

4.2. Computational Fluid Dynamics Results

All the operating conditions investigated experimentally were also analysed numerically, making it possible to clearly verify the variation in cooling performance associated with increasing flow rates and validate model results.

Table 2 reports the experimental and numerical results obtained for a water cooling flow rate of 1.2 l/min. The consistency of the results is demonstrated by the correspondence between CFD and experiments for the values of water outlet temperature $T_{w,o}$, the average temperature of the coil T_{Cu}, and the heat exchanged between the body and the coolant Q.

It may be relevant to specify that the experimental values Q are evaluated by means of the increase in temperature of the fluid from the water data, while the numerical values Q_{CFD} are evaluated as the integral of heat flow through the interface between the liquid and solid domains:

$$Q_{CFD} = \int_{S,conv} q \cdot dS_{conv} \tag{8}$$

$$Q = m \cdot cp \cdot (T_{w,o} - T_{w,i}) \tag{9}$$

where q is the local heat flux, m is the mass flow rate, and cp is the specific heat of the coolant.

Table 2: Comparison between experimental and numerical results obtained for a flow rate of 1.2 l/min.

J A/mm^2	$T_{w,o}$ $°C$	$T_{w,o,CFD}$ $°C$	T_{Cu} $°C$	$T_{Cu,CFD}$ $°C$	Q W	Q_{CFD} W
20	17.5	17.4	20.0	16.4	318	281
40	28.5	27.9	29.9	23.8	1256	1185
50	37.8	36.1	35.4	29.6	1984	1824
70	63.0	59.7	50.1	46.3	4144	3777
80	81.3	76.0	61.7	57.8	5643	5126

Figure 7 shows the temperature distribution in the three cooling coils operating at the same current supply of $50A/mm^2$ but subjected to different cooling flow rates. Despite identical load conditions, the coils exhibit markedly different thermal behaviours due to the distinct cooling regimes: 0.526 l/min in case (a), 1 l/min in case (b), and 1.2 l/min in case (c). The presented image reports contours of temperature distribution along the coils, highlighting a distinct temperature gradient developed along the coil in all cases. The outlet region copper temperature varies considerably between cases: approximately 35 °C in case (c), 40 °C in case (b), and 70 °C in case (a). In scenario (a), the diminished coolant flow results in elevated temperatures across the structure, with maximum values nearing 160 °C at the terminals, where there is an absence of direct liquid cooling. As the flow rate is augmented, a gradual decline in the maximum temperature is evident, thereby substantiating the enhanced thermal management accomplished through the augmentation of cooling. The consistent spatial pattern of the thermal fields and the physically coherent temperature trends confirm the reliability of the numerical setup and the robustness of the cooling model.

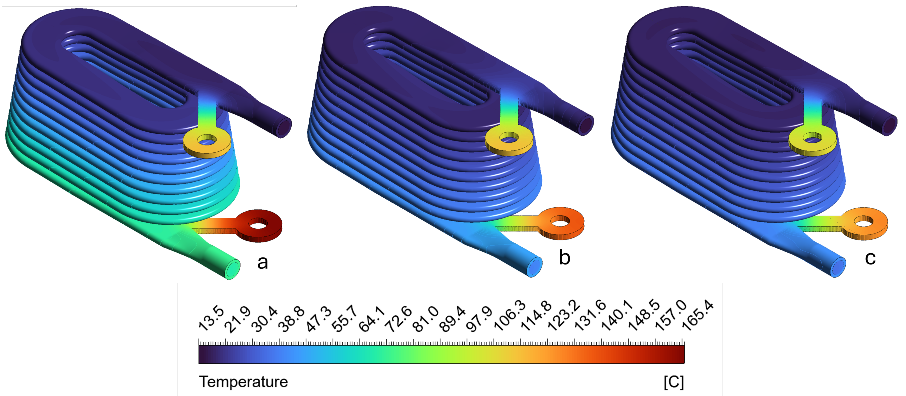

Figure 7: Temperature map corresponding to a flow rate of (a) 0.526, (b) 1.0 and (c) 1.2 l/min. Current density 50 A/mm^2

The differences observed among the three temperature fields directly reflect the variation of the effective heat-transfer coefficient associated with each cooling flow rate. As the flow increases, enhanced convective heat removal leads to lower peak temperatures and a more efficient overall thermal response. In addition, higher flow rates promote the transition toward a more turbulent regime within the coil, further increasing mixing and local heat exchange. This shift in flow behaviour contributes to the improved cooling effectiveness observed at larger mass flow rates. Indeed, multiple turns in coil geometry generate high resistance to the flow but also promote turbulent flow as the coolant flow rate increases. Turbulent or transient flow is expected, approaching a Reynolds number equal to 3140 at 1 l/min and 3768 at 1.2 l/min. However, laminar flow conditions are expected for flow rates up to 0.7 l/min, having a Reynolds number up to 2198. This condition mainly reflects the very small cross-sectional area of the configuration, having an equivalent hydraulic diameter of about 2 mm. These conditions also affect the pressure drop across the component, which is estimated to range between 0.6 and 1.3 bar and is a strong function of the flow conditions. In this case, the comparison with experimental data proves to be more challenging, primarily due to the difficulty in obtaining accurate evaluations of surface roughness within the coil internal duct. Overall, the numerical model is deeply validated, providing a precise tool with which to study and apply this type of cooling system.

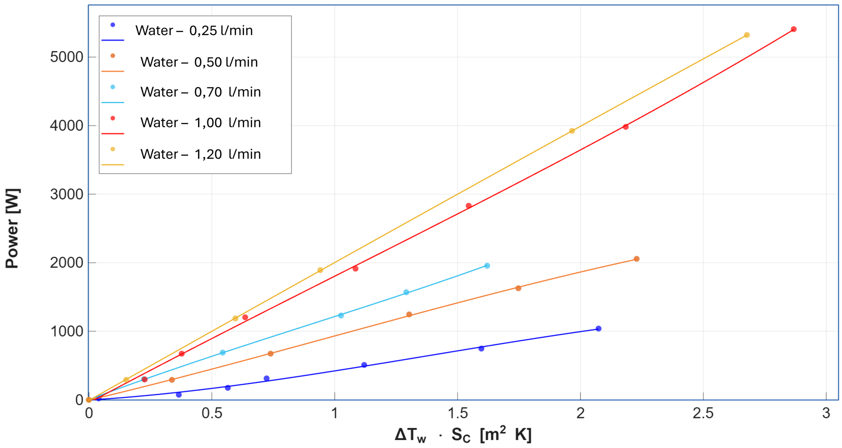

Figure 8: Delivered Power as function of $\Delta T_W \cdot S_{Conv}$. The slope of the lines represents the average heat transfer coefficient for different coolant flow rates, according to formulation in Eq.**??**.

Estimation and visualisation of the Heat Transfer Coefficient can be done in Figure 8. The image reports the delivered thermal power as a function of the component $\Delta T_W \cdot S_{Conv}$, corresponding to the product of the solid-liquid interface S_{Conv}, which is the source of convective heat transfer, and the consequent difference in temperature on water side between the inlet and outlet $\Delta T_W = T_{w,out} - T_{w,in}$. By definition, the ratio between the two reported physical quantities, corresponding to the slope of the obtained interpolation lines, represents the Heat Transfer Coefficient: $HTC = P/\Delta T_W \cdot S_{Conv}$. Measured and computed values of HTC find excellent agreement, as can be observed from Table 3, which reports corresponding values for all the tested flow rates. It's crucial to observe the superior performance obtained by water cooling with respect to the air case, which is the reason for the outstanding results obtained in terms of possible working current densities. However, these values still represent an improvement with respect to external air convection, traditionally reaching lower exchange values. Moreover, a significant step increase is observed between laminar (0.5 l/min) and turbulent flow cases (1.2 l/min), with the change in flow conditions resulting in almost doubling the heat exchange.

4.3. One Dimensional Model

The performance of the 1D Modelica model is evaluated in Table 4, which compares its temperature predictions against high-fidelity CFD results and experimental data at a constant flow rate of 1.2 l/min. Overall, the results demonstrate that the 1D Modelica model is a highly effective surrogate for predicting water outlet temperature (T_{OUT}), maintaining strong alignment with both the CFD results and experimental data across the full range of current densities. Instead, pressure losses are significantly more sensitive to localised geometric features, such as sharp bends, surface roughness, and 3D flow

Table 3: Experimental and numerically computed HTC.

$Flow\ rate$ l/min	$Coolant\ Fluid$	HTC_{EXP} W/m^2K	HTC_{CFD} W/m^2K
0.25	water	442	419
0.526	water	930	926
0.75	water	1238	1226
1.0	water	1768	1769
1.2	water	2122	2094

Table 4: Water outlet temperature evaluated throu .

$Flow\ rate$ l/min	$Current\ Density$ A/mm^2	T_{OUT} $°C$	$T_{OUT,CFD}$ $°C$	$T_{OUT,MODELICA}$ $°C$
1.2	20	17.5	17.4	17.36
1.2	40	28.5	27.9	27.9
1.2	50	37.8	36.1	36.94
1.2	70	63	59.7	60.56
1.2	80	81.3	76.0	77.6

structures, which are inherently simplified in a 1D lumped-parameter framework, resulting in considerable overestimations.

The adoption of a 1D lumped-parameter approach provides a strategic balance between computational efficiency and predictive accuracy. Unlike high-fidelity CFD simulations, the 1D model facilitates rapid iterative cycles and near real-time performance.

5. Electromagnetic Design

The impact of a directly cooled winding for a Surface-mounted Permanent Magnet (SPM) motor and for a Reluctance (REL) motor is now briefly described. A thorough investigation on the effects of this device on these two types of motors is presented in [16]. That study shows that by adopting the directly fluid cooled hollow conductors, the current density may be increased by a factor of between 2 and 3. This significant advantage is the main reason behind the choice to study the performance of the winding directly cooled by CFD analyses.

The same outer stator is considered as initial condition. Since the iron path is typically designed to obtain the maximum magnetic loading, it is possible to consider the back iron height and the stator tooth width as constant. The electric loading of the SPM and REL motors may be expressed as:

$$\hat{K}_s = \frac{k_w \sqrt{2} J_s h_s w_s k_{fill}}{\pi D / Q_s} \tag{10}$$

where k_w and k_{fill} are the winding and slot fill factors, h_s and w_s are the height and width of the slot, Q_s is the number of slots, D is the stator inner diameter, and J_s is the *rms* of the current density (directly proportional to the $K_s D$ term). By its side, $K_s D$ product is directly proportional to the motor torque, as shown in equation 11:

$$T = \frac{\pi}{4} D L_{stk} \hat{B} (\hat{K}_s D) \tag{11}$$

with L_{stk} stack length and $\hat{B}$ flux density.

In the SPM motor, the PM flux density variation ΔB is defined by the following equation:

$$\Delta B = \mu_0 \frac{\hat{K}_s D}{2p(g + t_m/\mu_{rec})} \tag{12}$$

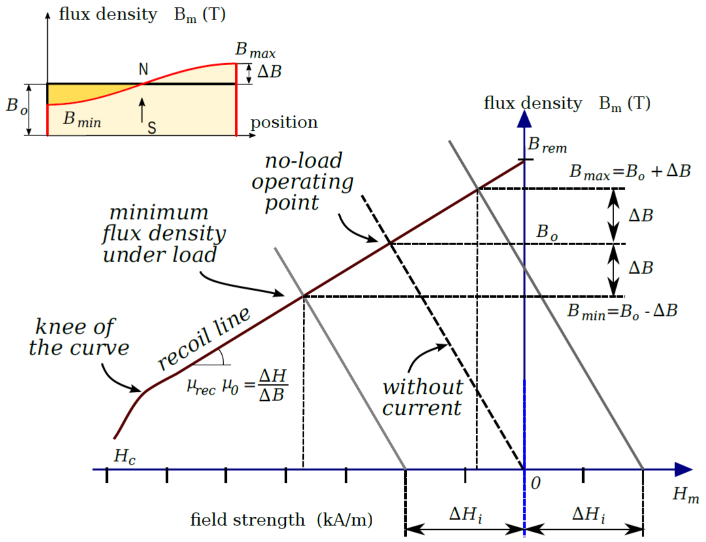

Figure 9: Current reaction on the PM and the corresponding BH curve with hypothesis of sinusoidal variation of the current reaction.

p is the number of pole pairs, g is the air-gap thickness, t_m is the PM thickness, and μ_{rec} is the recoil permeability of the PM material.This parameter is important because an increase in the electric loading leads to a reduction in the PM flux density, causing possible irreversible demagnetisation. To avoid this phenomenon, it is necessary to raise the PM thickness and also the air-gap, if needed.

Figure 9 shows the flux density distribution in the PM and the corresponding variation in the PM BH curve. It shows that the flux density is not constant along the PM surface and that, to avoid PM demagnetisation, the minimum flux density must not reach the knee of the BH curve. For both SPM and REL motor cases, a Finite Element Analysis (FEA) verification has been conducted. Results prove that:

1. In the SPM motor case, the negligible growth of the average flux density with t_m shows that the increase in the average torque depends on the rise in the current and not on the increase in PM mass.
2. The REL motor, considering the same operating conditions, exhibits a torque that is approximately 80% of the torque that the SPM motor produces with the same stator and current.
3. While in PM motors, the high torque requires an increase of the PM volume and mass, the REL motor may develop a high torque without requiring an additional cost (according to a high cooling of the conductors).

6. Conclusions

This study demonstrates that the integration of additive manufacturing technology with internally cooled hollow copper conductors represents a transformative advancement in the thermal management of high-power electric machines. By embedding forced liquid cooling directly within the windings, the proposed architecture effectively decouples electromagnetic loading from conventional thermal constraints, enabling a substantial increase in current densities and a 2.5-fold increase in torque density compared to state-of-the-art externally cooled systems. The strong correlation observed between experimental measurements and numerical predictions—validated through both high-fidelity CFD simulations and efficient 1D lumped-parameter models—confirms the reliability and scalability of the proposed framework. Ultimately, this work establishes a robust methodology for the design of next-generation energy conversion systems, laying the groundwork for further geometric optimisation and the exploration of diverse machine topologies enabled by the design freedom of additive manufacturing

References

[1] Wang, Q., Wu, Y., Niu, S., Zhao, X. *Advances in thermal management technologies of electrical machines.* Energies, 15(9), 3249.

[2] Mellor, P. H., Roberts, D., Turner, D. *Lumped parameter thermal model for electrical machines of tefc design.* IEE Proceedings B (Electric Power Applications), 138(5), 205–218.

[3] Sarma, N., Kulan, M. C., Baker, N. J. *A comprehensive review of thermal conductivity of stator windings in electric machines.* IEEE Access.

[4] Chai, F., Cao, Y., Pei, Y. *Design and analysis of high torque density permanent magnet synchronous motor based on heat pipe.* 2022 25th International Conference on Electrical Machines and Systems (ICEMS), 1–6.

[5] Cakal, G., Sarlioglu, B. *Review of advances in cooling schemes for yokeless and segmented armature (yasa) axial flux motors.*. 2023 25th European Conference on Power Electronics and Applications (EPE'23 ECCE Europe), 1–8.

[6] Madhavan, S., P B, R., Gundabattini, E., Mystkowski, A. *Thermal analysis and heat management strategies for an induction motor, a review.* Energies, 15, 8127. https://doi.org/10.3390/en15218127

[7] Ponomarev, P., Polikarpova, M., Pyrh¨onen, J *Thermal modeling of directly-oil-cooled permanent magnet synchronous machine.*

[8] Yao, Z., Mandel, R. K., P., M. F. *In-slot cooling for high power density electric motor with encapsu- lation channels.* 21st IEEE Intersociety Conference on Thermal and Thermomechanical Phenomena in Electronic Systems (iTherm), 978-1-6654-8503-6. https://doi.org/10.1109/iTherm54085.2022.9899559

[9] Nonneman, J., T'Jollyn, I., Clarie, N., Weckx, S., Sergeant, P., De Paepe, M. *Model-based comparison of thermo-hydraulic performance of various cooling methods for power electronics of electric vehicles.* 17th IEEE ITHERM Conference, 78-1-5386-1272-9.

[10] Ghahfarokhi, P. S., Podgornovs, A., Cardoso, A. J. M., Nelahcen, A., Tiismus, H. *Opportunities and challenges of utilizing additive manufacturing approaches in thermal management of electrical machines.*. IEEE Access, 9, 36368–36381. https://doi.org/10.1109/ACCESS.2021.3062618 .

[11] Wu, F., EL-Refaie, A. M. *Toward additively manufactured electrical machines: Opportunities and challenges.* IEEE TRANSACTIONS ON INDUSTRY APPLICATIONS, 56(2).

[12] Pecotivh, J., Klink, D., Heins, G., Bahrani, B. *Additively manufactured electric machine conductors with integrated end turn cooling.*. EEE TRANSACTIONS ON INDUSTRY APPLICATIONS, 61(4), 6183–6192.

[13] Comitato Elettrotecnico Italiano. *Isolamento elettrico - valutazione e classificazione termica.* (tech. rep.No. CEI EN 60085) (Recepimento della norma internazionale IEC 60085). CEI. Milano, Italia.

[14] Ansys Inc. *Ansys fluent user's guide, release 2025 R1.* Ansys, Inc. Canonsburg, PA, USA. https://ansyshelp.ansys.com

[15] Di Gerlando, A., Foglia, G., Ricca, C. *Analytical design of a high torque density in-wheel yasa afpm motor.* 2020 International Conference on Electrical Machines (ICEM), 1, 402–408.

[16] Bianchi, N., De Gregorio, D., Filippini, F., Di Leonardo, L., Sech, E., Stoppato, A., Tripaldi, F., Rossi, A. *Enhanced torque density in electric motors through liquid-cooled hollow conductors.*. 2025 IEEE Energy Conversion Conference Congress and Exposition (ECCE), 1–8.